



# Novel $\alpha$ -FeOOH corner-truncated tetragonal prisms: crystal structure, growth mechanism and lithium storage properties

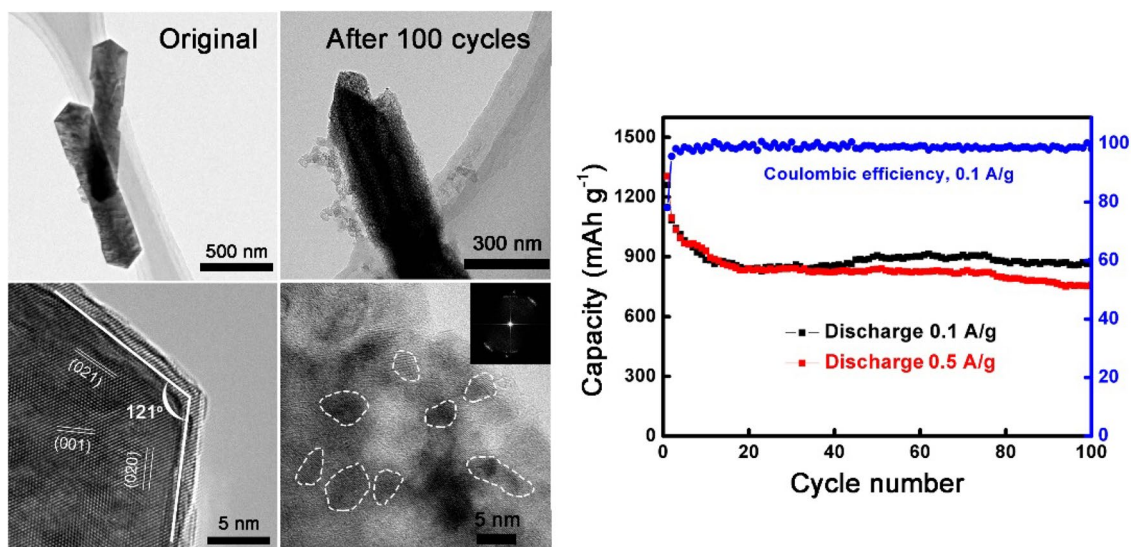
Huanqing Liu<sup>1</sup> · Jiajia Zou<sup>1</sup> · Yanhua Ding<sup>1</sup> · Bing Liu<sup>1</sup> · Yiqian Wang<sup>1</sup>

Received: 17 October 2018 / Accepted: 26 April 2019 / Published online: 15 May 2019  
© Springer Nature B.V. 2019

## Abstract

Novel goethite ( $\alpha$ -FeOOH) corner-truncated tetragonal prisms (CTPs) with a length of about 1  $\mu\text{m}$  and a width of about 200 nm have been synthesized by a hydrothermal method. The morphology, structure and electrochemical properties of CTPs are systematically studied. The obtained  $\alpha$ -FeOOH CTPs exhibit high-quality single-crystalline nature. In addition, the single  $\alpha$ -FeOOH corner-truncated tetragonal prism (CTP) is enclosed by six side facets, two {020} and four {110}. Depending on the reaction time, two different types of top-endings, one flat or two canted facets, are obtained. The formation of  $\alpha$ -FeOOH is associated with the growth and subsequent phase transformation of  $\beta$ -FeOOH. The CTP contributes to structural stability and avoids the common pulverization process of electrodes. In addition, tiny crystallites are generated during the cycle, which increase the contact area between the electrode and electrolyte. Therefore, the  $\alpha$ -FeOOH CTPs electrode displays excellent cycling performance with a reversible specific capacity of 870  $\text{mAh g}^{-1}$  at 100  $\text{mA g}^{-1}$  after 100 cycles.

## Graphical abstract



**Keywords** Lithium-ion batteries ·  $\alpha$ -FeOOH · Corner-truncated tetragonal prism structure · Growth mechanism · Surface-controlled capacitive

✉ Bing Liu  
bing\_liu@qdu.edu.cn

✉ Yiqian Wang  
yqwang@qdu.edu.cn

Extended author information available on the last page of the article

## 1 Introduction

Rechargeable lithium-ion batteries (LIBs) have received increasing attention because of the wide range of applications from portable electronic devices to electric vehicles and electric grids [1–3]. To meet market demands, considerable efforts have been made by the scientific community to develop advanced electrode materials. Among the available anode materials, iron (hydr)oxides have attracted tremendous attention due to their higher capacity than that of commercial graphite anodes ( $372 \text{ mAh g}^{-1}$ ) and intrinsically enhanced safety. The capacity of lithium storage can be mainly achieved through the reversible conversion reaction between  $\text{Li}^+$  and oxides [4–9]. As a most widely distributed iron oxide, goethite ( $\alpha\text{-FeOOH}$ ) has been studied as promising candidates for high theoretical capacity, abundant resource and environmental friendliness [10–13].

Nanoscale  $\alpha\text{-FeOOH}$  materials with anisotropic morphology and structure possess unique physical and chemical properties [14–17]. Intensive efforts have been devoted to preparation and modification of  $\alpha\text{-FeOOH}$  nanostructures. At present, researchers have reported many one-dimensional (1D)  $\alpha\text{-FeOOH}$  nanostructures, such as needles, nanowires, and nanorods [18–20]. Lou et al. [21] reported a facile one-pot glucose-mediated hydrothermal method for the synthesis of  $\text{FeOOH}$  rod-like nanoparticles. They converted the  $\text{FeOOH}$  nanoparticles into carbon-coated magnetite ( $\text{Fe}_3\text{O}_4@\text{C}$ ) nanocomposite, which exhibited good cycling performance. The  $\alpha\text{-FeOOH}$  materials with diverse morphology are prepared by scientists to enhance their performance, such as spindles [22], x-shaped hollow  $\alpha\text{-FeOOH}$  penetration twins [23]. In addition, researchers tried to boost the electrochemical properties of  $\alpha\text{-FeOOH}$  by adding conductive graphene. For example, microcrystalline  $\alpha\text{-FeOOH}/\text{rGO}$  samples have been successfully synthesized, which display superior performance with a reversible capacity of  $569 \text{ mAh g}^{-1}$  after 50 cycles [24]. However, the preparation of  $\alpha\text{-FeOOH}$  with unique morphology and structure remains a challenge. In terms of  $\alpha\text{-FeOOH}$  1D nanostructures, it is of great significance to prepare  $\alpha\text{-FeOOH}$  with novel morphology for practical applications.

Herein, we synthesize novel  $\alpha\text{-FeOOH}$  corner-truncated tetragonal prisms (CTPs) with a length of about  $1 \mu\text{m}$  and a width of about  $200 \text{ nm}$  through a facile hydrothermal method. The single-crystalline  $\alpha\text{-FeOOH}$  exhibits six symmetric side facets. The top-ending of corner-truncated tetragonal prism (CTP) shows two different types, one being flat, and the other being two canted facets. Time-dependent experiments of crystal growth are also performed to obtain detailed information of morphological evolution. Benefiting from its unique structural features, the  $\alpha\text{-FeOOH}$  electrode exhibits good lithium storage performance for LIBs.

## 2 Experimental

### 2.1 Synthesis of $\alpha\text{-FeOOH}$ CTPs

All chemicals are of analytical grade and used without further purification. Deionized water was used throughout the experiment. The  $\alpha\text{-FeOOH}$  CTPs were fabricated through a simple hydrothermal treatment of precursor solution. In detail,  $2 \text{ mmol}$  of  $\text{FeCl}_3 \cdot 6\text{H}_2\text{O}$  was dissolved in a solution of deionized water ( $15 \text{ mL}$ ) and ethanol ( $15 \text{ mL}$ ), and  $1.2 \text{ g}$  of polyvinyl pyrrolidone (PVP) was also dissolved in the same solution. Then,  $30 \text{ mL}$  of PVP solution was added into  $\text{FeCl}_3$  solution under magnetic stirring to form a homogeneous solution. After that,  $125 \mu\text{L}$  of  $\text{NH}_3 \cdot \text{H}_2\text{O}$  was added to the above mixture solution under vigorous stirring for  $15 \text{ min}$ , and  $0.47 \text{ mol/L}$   $\text{NH}_4\text{F}$  aqueous solution ( $20 \text{ mL}$ ) was further added to the suspension under stirring for  $10 \text{ min}$ . Subsequently, the resulting solution was transferred into a  $100 \text{ mL}$  Teflon-lined stainless steel autoclave and then maintained at  $180 \text{ }^\circ\text{C}$  for several hours. After cooling to ambient room temperature naturally, the yellow precipitate was collected by centrifugation. The resulting precipitate was washed three times with deionized water and ethanol, and dried at draught cupboard. To further study the growth mechanism of the product, the hydrothermal experiments were performed under the same conditions except the reaction time.

### 2.2 Material characterization

The phase analysis was carried out using X-ray powder diffraction (SmartLab XRD) with  $\text{Cu-K}\alpha_1$  radiation ( $\lambda = 1.5406 \text{ \AA}$ ). The sample morphologies were characterized by scanning electron microscope (SEM, Hitachi S-4800). Bright-field (BF) images, high-resolution transmission electron microscopy (HRTEM) images and selected-area electron diffraction (SAED) patterns were recorded on a JEOL JEM 2100F transmission electron microscope (TEM) operating at  $200 \text{ kV}$ . The Brunauer–Emmett–Teller (BET) method was used to calculate the specific surface area from the desorption branches of the isotherms. The FT-IR spectra of samples were recorded on a Fourier transform infrared spectrometer (Thermo Scientific Nicolet iS50).

### 2.3 Electrochemical measurement

The electrochemical properties of the as-prepared  $\alpha\text{-FeOOH}$  CTPs were evaluated using a coin cell with lithium metal as a counter electrode. The working electrode was prepared by pressing a mixture of sample powder ( $70 \text{ wt\%}$ ), acetylene black ( $15 \text{ wt\%}$ ) and water-soluble sodium alginate (SA,  $15 \text{ wt\%}$ ) onto a copper foil and subsequently dried at  $80 \text{ }^\circ\text{C}$  for a whole night in a vacuum oven. The electrolyte

consisted of 1 M  $\text{LiPF}_6$  solution of ethylene carbonate (EC)/diethyl carbonate (DEC) (1:1 in volume). The coin-type cell of CR2025 was then assembled in a glove box filled with pure argon gas with a moisture and oxygen concentration of less than 0.1 ppm. The average mass loading of  $\alpha\text{-FeOOH}$  for cell testing was  $0.72 \text{ mg cm}^{-2}$ . Cyclic voltammetry (CV) profiles were obtained between 0.01 and 3.00 V using an electrochemical workstation (PGSTAT 302 N). Galvanostatic discharge/charge measurements were performed on a lithium battery test system (LAND CT2001) with a potential range of 0.01–3.00 V versus  $\text{Li}^+/\text{Li}$ . Electrochemical impedance spectroscopy (EIS) tests were performed on a Metrohm Autolab electrochemical workstation (PGSTAT 302 N) with a frequency range from 100 kHz to 0.01 Hz.

### 3 Results and discussion

The phase of as-synthesized samples was determined using XRD, as shown in Fig. 1a. All the diffraction peaks of the as-synthesized sample can be indexed to orthorhombic  $\alpha\text{-FeOOH}$  (JCPDS No.: 81-0462), confirming the single-phase characteristics of the product [25]. No other peaks from impurities were found, suggesting the high purity of the products. The morphology of  $\alpha\text{-FeOOH}$  was characterized by field-emission SEM. As can be seen from Fig. 1b, uniform  $\alpha\text{-FeOOH}$  prisms are synthesized by hydrothermal process. These prisms have a length of about 1  $\mu\text{m}$  and a width of about 200 nm, and has smooth side facet. Figure 1c,

d display enlarged top views of a single prism. Interestingly, two different types of top-endings can be observed, one being flat and the other being two canted facets. Moreover, it can be clearly seen that each prism has six symmetrical sides with a width of about 100 nm.

To better illustrate the unique structure, the microstructure of the  $\alpha\text{-FeOOH}$  prisms was examined by TEM. Figure 2a shows a typical BF TEM image of  $\alpha\text{-FeOOH}$  prisms. The uniform  $\alpha\text{-FeOOH}$  prisms with different top-endings are observed, which is consistent with SEM observation. Figure 2b shows HRTEM image of an individual  $\alpha\text{-FeOOH}$  prism with a flat top surface, which is taken from the region enclosed by a red rectangle in Fig. 2a. The crystal lattice spacings were measured to be 4.08 Å and 2.95 Å, which can be identified as (110) and (001) of  $\alpha\text{-FeOOH}$ , respectively. The preferential growth along the  $c$ -axis with high energy facets is consistent with a kinetic growth mode [26]. The inset in Fig. 2b is the corresponding SAED pattern, which can be indexed to single-crystalline orthorhombic  $\alpha\text{-FeOOH}$  projected along the  $[\bar{1}10]$  zone-axis. Figure 2c shows an atomic model of the  $\alpha\text{-FeOOH}$  prism enclosed by (001) end facet and (110) side facet. It can be seen that the profile of the  $\alpha\text{-FeOOH}$  prism is in good agreement with the atomic model. Based on the above TEM results, it is concluded that the  $\alpha\text{-FeOOH}$  prism with a flat top-ending is enclosed by side facets of {110} and top facets of {001} (Fig. 2d).

The microstructure of  $\alpha\text{-FeOOH}$  prism with canted top-endings was studied by TEM to elucidate the exposed facets. Figure 3a clearly shows the top-endings with two canted

**Fig. 1** a XRD pattern and b typical SEM image of as-synthesized product. c, d Enlarged top views of individual prisms

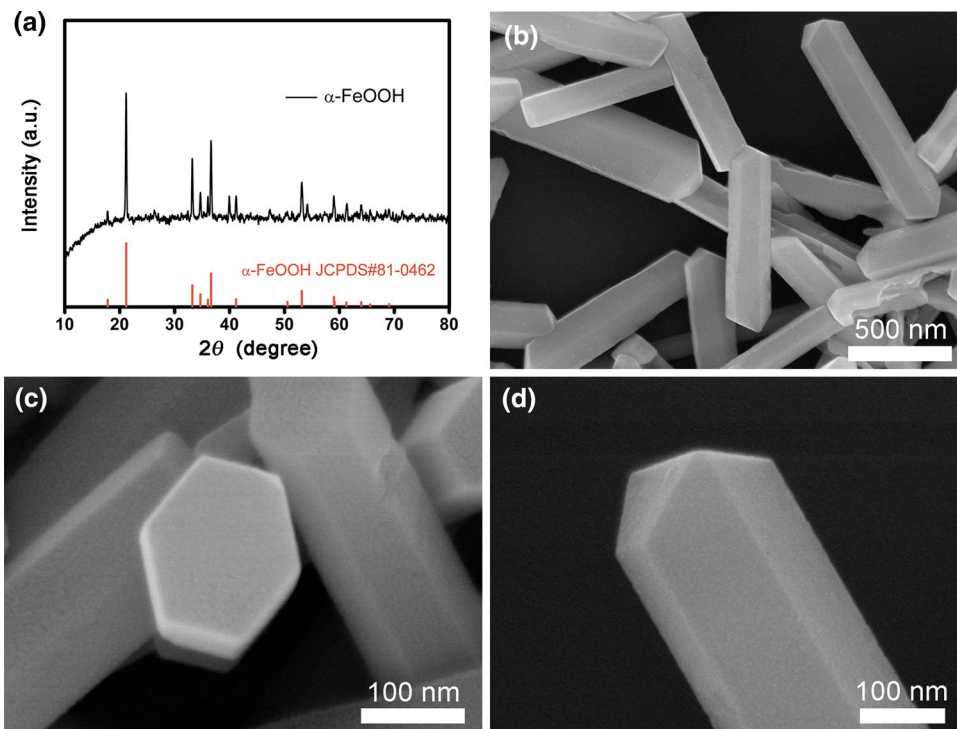
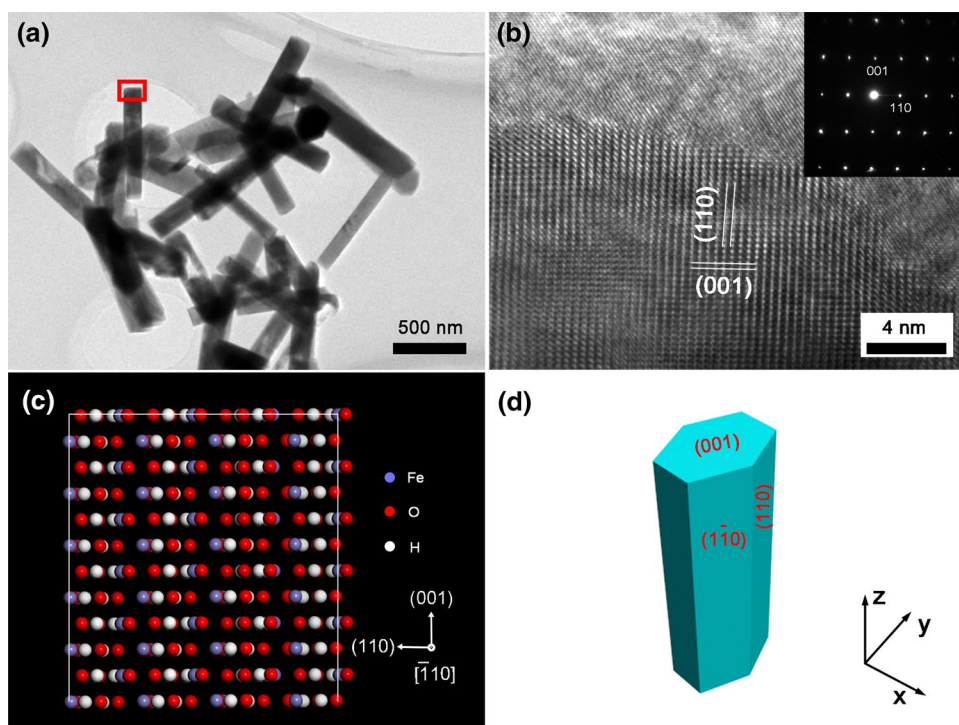


**Fig. 2** **a** Typical BF TEM image of  $\alpha$ -FeOOH prisms. **b** HRTEM image of the  $\alpha$ -FeOOH prism along the  $[\bar{1}10]$  direction, inset is corresponding SAED pattern. **c** Schematic atomic model of  $\alpha$ -FeOOH prism along  $[\bar{1}10]$  direction. **d** 3D geometrical model of  $\alpha$ -FeOOH prism with flat top-ending



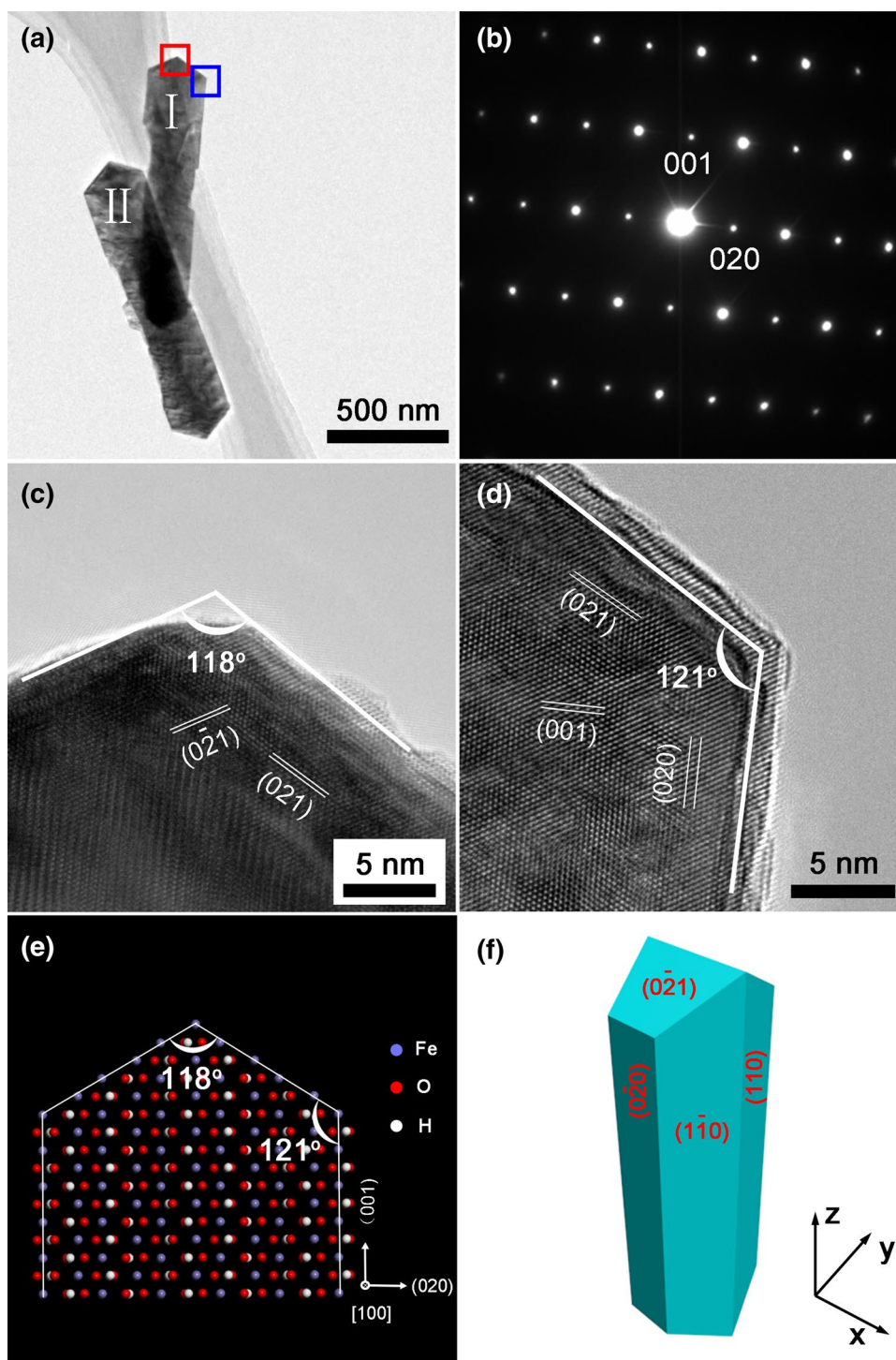
facets of  $\alpha$ -FeOOH prism. The  $[100]$  zone-axis SAED pattern of  $\alpha$ -FeOOH prism labeled I confirms its single-crystalline nature, as shown in Fig. 3b. As can be seen from the HRTEM image taken from the region enclosed by a red rectangle in Fig. 3a, the top-endings of  $\alpha$ -FeOOH prism are surrounded by  $(021)$  and  $(0\bar{2}1)$  facets, and the dihedral angle is measured to be  $118^\circ$ , which is consistent with the calculated value. Figure 3d shows a HRTEM image from the region enclosed by a blue rectangle to demonstrate the exposed side facets of the  $\alpha$ -FeOOH prism. The lattices with a spacing of  $4.97 \text{ \AA}$ , parallel to the  $c$ -axis direction of the prism, correspond to  $(020)$  facet. The angle between the side and the top facet is  $121^\circ$ , which is consistent with the theoretical angle between  $(020)$  and  $(021)$  planes. The profiles and angles of the  $\alpha$ -FeOOH prism are in good agreement with the atomic model of  $\alpha$ -FeOOH prism projected along the  $[100]$  direction, which is tailored by  $\{020\}$  and  $\{021\}$  facets (Fig. 3e). After careful examination of TEM images, a 3D geometrical model of  $\alpha$ -FeOOH with CTP structure was constructed. It can be seen from the model that the  $\alpha$ -FeOOH CTP with canted top-endings is enclosed by four  $\{110\}$  and two  $\{020\}$  facets, and capped by  $\{021\}$  facets.

In our case,  $\alpha$ -FeOOH CTPs with two different top-endings are synthesized under the conditions of high concentration of  $F^-$  and alkaline. Indeed,  $F^-$  could preferentially adsorb on the  $(110)$  facet due to the highest density of Fe atoms on the  $(110)$  facet, resulting in the lowest growth rate of  $(110)$  facet, which explains the appearance of four  $\{110\}$  side facets [24, 27]. The  $\{020\}$  facets are also found

to form easily in alkaline surroundings. Therefore,  $\alpha$ -FeOOH with six side facets can be produced under the condition of high-concentration ammonia in the synthetic solution. On the other hand, the commonly developed top-endings in synthetic goethite are the  $\{001\}$  facets. The high-energy  $\{021\}$  surfaces are often apex facets of needle-shaped goethite nanorods, especially in a strong alkaline environment [26, 28]. Typically, the crystal grows at the same speed along the  $b$ -axis and  $a$ -axis, in which the prism is capped by  $\{001\}$  facets. If the crystal grows faster along the  $a$ -axis than along the  $b$ -axis, the  $\{021\}$  facets can be obtained. Thus,  $\alpha$ -FeOOH with two different top-endings can be obtained.

To obtain detailed information of morphological evolution of  $\alpha$ -FeOOH CTPs, time-dependent experiments (1 h, 2 h, 3 h and 6 h) of crystal growth were performed. The phase of as-synthesized samples was investigated by XRD, as shown in Fig. 4. The sample with a reaction time of 1 h shows unambiguous diffraction peaks, which can be indexed to tetragonal  $\beta$ -FeOOH phase (JCPDS No.: 75-1594) [29]. The corresponding SEM image analysis (Fig. 5a) shows that a great many  $\beta$ -FeOOH nanoparticles (NPs) with an average size of 15 nm were synthesized. After 2 h of hydrothermal reaction, plenty of aggregations are clearly observed in Fig. 5b. In addition, a few rod-like constructions with larger size can be found. The XRD pattern of product with the reaction time of 2 h displays exclusive peaks of  $\beta$ -FeOOH, demonstrating that most aggregations are still  $\beta$ -FeOOH phase. As the reaction time increased to 3 h, the diffraction peaks of orthorhombic  $\alpha$ -FeOOH (labeled by \* in Fig. 4)

**Fig. 3** **a** Magnified TEM image of  $\alpha$ -FeOOH prism with canted facets. **b** SAED pattern of single crystal  $\alpha$ -FeOOH prism. **c, d** HRTEM images of the  $\alpha$ -FeOOH prism taken from red and blue square frame in (a). **e** Schematic atomic model of an ideal  $\alpha$ -FeOOH prism projected along [100] direction. **f** 3D geometrical model of  $\alpha$ -FeOOH prism with canted facets



appear. Figure 5c is the corresponding SEM image. It can be seen that the sample consists of prisms with irregular surface and a small number of nanoparticles. When the reaction time is further prolonged to 6 h, all diffraction peaks can be indexed to  $\alpha$ -FeOOH phase. The SEM image (Fig. 5d) shows that uniform  $\alpha$ -FeOOH CTPs with a length of about 1  $\mu\text{m}$  and a width of about 200 nm are obtained, and at the same time, the nanoparticles disappear. Therefore, the sample

obtained by 3 h hydrothermal reaction consists of  $\alpha$ -FeOOH prisms and  $\beta$ -FeOOH NPs. The above results reveal that the  $\alpha$ -FeOOH prisms grow at the expense of  $\beta$ -FeOOH NPs, which is similar to the reports in previous literature [24, 30].

The as-prepared FeOOH samples were also examined using FT-IR spectra to demonstrate phase transformation process of  $\beta$ -FeOOH. The FT-IR spectrum of the sample with a reaction time of 1 h shows two absorption peaks at

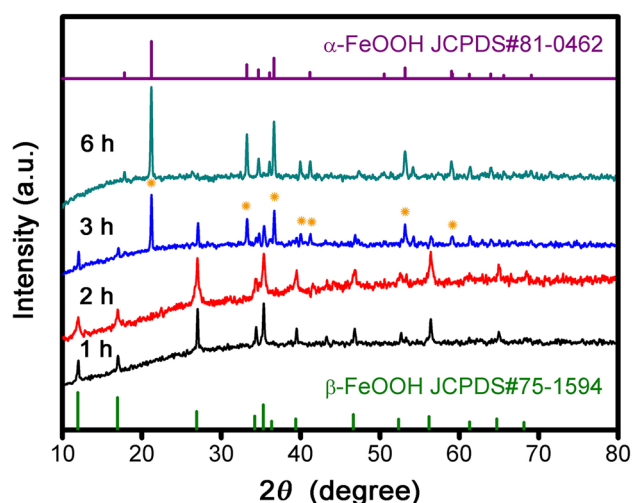


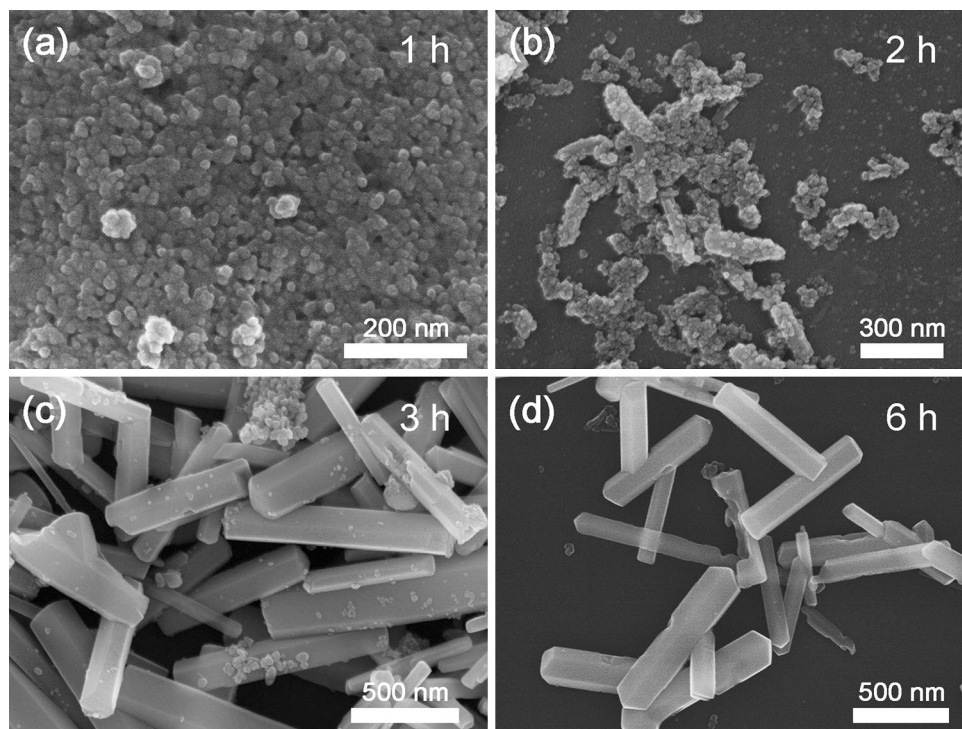
**Fig. 4** XRD patterns of as-synthesized FeOOH with different reaction times

687 and 836  $\text{cm}^{-1}$  (Fig. 6a), which are assigned to the Fe–O vibrational mode in  $\beta$ -FeOOH [31]. After 2 h, hydrothermal reaction, the FT-IR spectrum of samples exhibits similar absorption band compared with the samples with a reaction time of 1 h. The experimental results confirm that the  $\beta$ -FeOOH continues to grow during this stage, and the phase transformation has not yet occurred. For the FT-IR spectra of the sample with a synthesis time of 3 h, besides the presence of typical bands of  $\beta$ -FeOOH (687 and 836  $\text{cm}^{-1}$ ),

three absorption bands at 871  $\text{cm}^{-1}$ , 775  $\text{cm}^{-1}$ , and 637  $\text{cm}^{-1}$  are observed. These peaks can be attributed to the Fe–O–H bending vibration and the Fe–O stretching vibration of  $\alpha$ -FeOOH, indicating the presence of the  $\alpha$ -FeOOH phase [32]. As reaction time is extended to 6 h, an intense band at about 3158  $\text{cm}^{-1}$  appears, which can be ascribed to the O–H stretching mode in  $\alpha$ -FeOOH, while the peak at 3468  $\text{cm}^{-1}$  can be attributed to stretching modes of surface  $\text{H}_2\text{O}$  and the envelope of hydrogen-bonded surface OH groups [33]. Two typical bands of 883 and 781  $\text{cm}^{-1}$  can be attributed to the Fe–O–H bending vibration of  $\alpha$ -FeOOH. The Fe–O stretching vibrations are responsible for the bands at 628  $\text{cm}^{-1}$ . The FT-IR spectra further demonstrate that the product transforms from tetragonal  $\beta$ -FeOOH to orthorhombic  $\alpha$ -FeOOH crystals, and the pure  $\alpha$ -FeOOH sample is obtained after 6 h of hydrothermal process.

To further investigate the growth mechanism of  $\alpha$ -FeOOH prisms, the as-synthesized samples obtained under hydrothermal conditions of 1, 2 and 3 h, were characterized by TEM. Initially, the large aggregate of primary particles is observed in Fig. 7a, which consists of many small particles with a pseudo-spherical shape and a size < 15 nm. Lattice fringes visible in the HRTEM image (Fig. 7b) have spacing corresponding to  $\beta$ -FeOOH (130) plane, consistent with the XRD and SEM results. The TEM image of 2 h sample shows that the aggregation of primary particles appears. The HRTEM image (Fig. 7d) shows that lattice fringes (about 3.31 and 2.60 Å) correspond to the (130) and (400) facets of the tetragonal  $\beta$ -FeOOH, respectively. The amorphous

**Fig. 5** SEM images of as-synthesized samples with reaction times of 1 h (a), 2 h (b), 3 h (c), and 6 h (d)



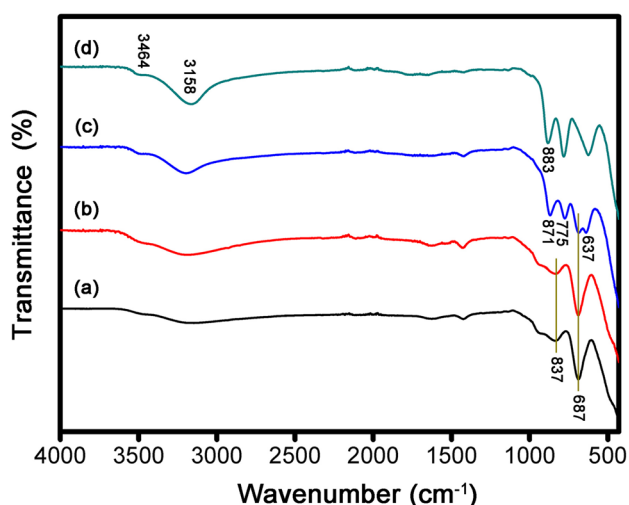


**Fig. 6** FT-IR spectra of FeOOH samples synthesized with reaction times of 1 h (a), 2 h (b), 3 h (c), and 6 h (d)

boundaries between adjacent nanoparticles are visible. The edge of aggregate consists of a number of  $\beta$ -FeOOH NPs, suggesting that the phase transformation from  $\beta$ -FeOOH into  $\alpha$ -FeOOH is related to the aggregation of  $\beta$ -FeOOH, which is different from the previous reports [34–36]. After 3 h, rod-shaped samples can be clearly seen in Fig. 7e. Many particles with a size of  $\sim 10$  nm are attached to the surface. The HRTEM image in Fig. 7f displays an interplanar spacing of 2.53 Å for the (211) facets of  $\beta$ -FeOOH, which is in good agreement with above SEM results. Moreover, a good crystalline prism can be found in Fig. 7g, while Fig. 7h displays its HRTEM image. The lattice spacing of 4.96 Å corresponds to the (020) facet of  $\alpha$ -FeOOH, confirming the coexistence of  $\beta$ -FeOOH and  $\alpha$ -FeOOH. The above results reveal that the formation of  $\alpha$ -FeOOH CTPs is involved in the growth and subsequent phase transformation of  $\beta$ -FeOOH.

Based on the above results, a growth process of  $\alpha$ -FeOOH CTPs is proposed, as shown in Fig. 8. Initially, numerous  $\beta$ -FeOOH NPs form under hydrothermal conditions (Fig. 5a). These particles continue to grow over time. After 2 h, many large  $\beta$ -FeOOH particles begin to aggregate (Fig. 5b). Such aggregate-like particle morphologies are often found in nanoparticle system produced by aggregation [37, 38]. Indeed, akaganeite has lower nucleation energy, thus growing faster than goethite. However, goethite becomes more stable compared to akaganeite in the subsequent growth process because it has relatively low free energy [4, 39]. In our case, akaganeite is formed earlier than goethite. Then, akaganeite particles aggregate until the resultant particles reach a size where transformation to goethite is thermodynamically favorable (Fig. 7c). The formation of the early-stage goethite prism can be driven by aggregation of akaganeite particles. As the hydrothermal reaction proceeds,  $\alpha$ -FeOOH prism grows

continuously, and the  $\beta$ -FeOOH NPs are consumed by the dissolution/recrystallization process, which is consistent with previous report [40]. After 6 h of hydrothermal reaction, well-defined  $\alpha$ -FeOOH CTPs can be obtained. In addition, the nitrogen adsorption/desorption isotherm curves of  $\alpha$ -FeOOH are shown in Fig. 9. The BET surface area of  $\alpha$ -FeOOH is found to be  $7.1 \text{ m}^2 \text{ g}^{-1}$ . The  $\alpha$ -FeOOH CTP is expected to exhibit good lithium storage properties due to high-activity side surfaces. [26, 28].

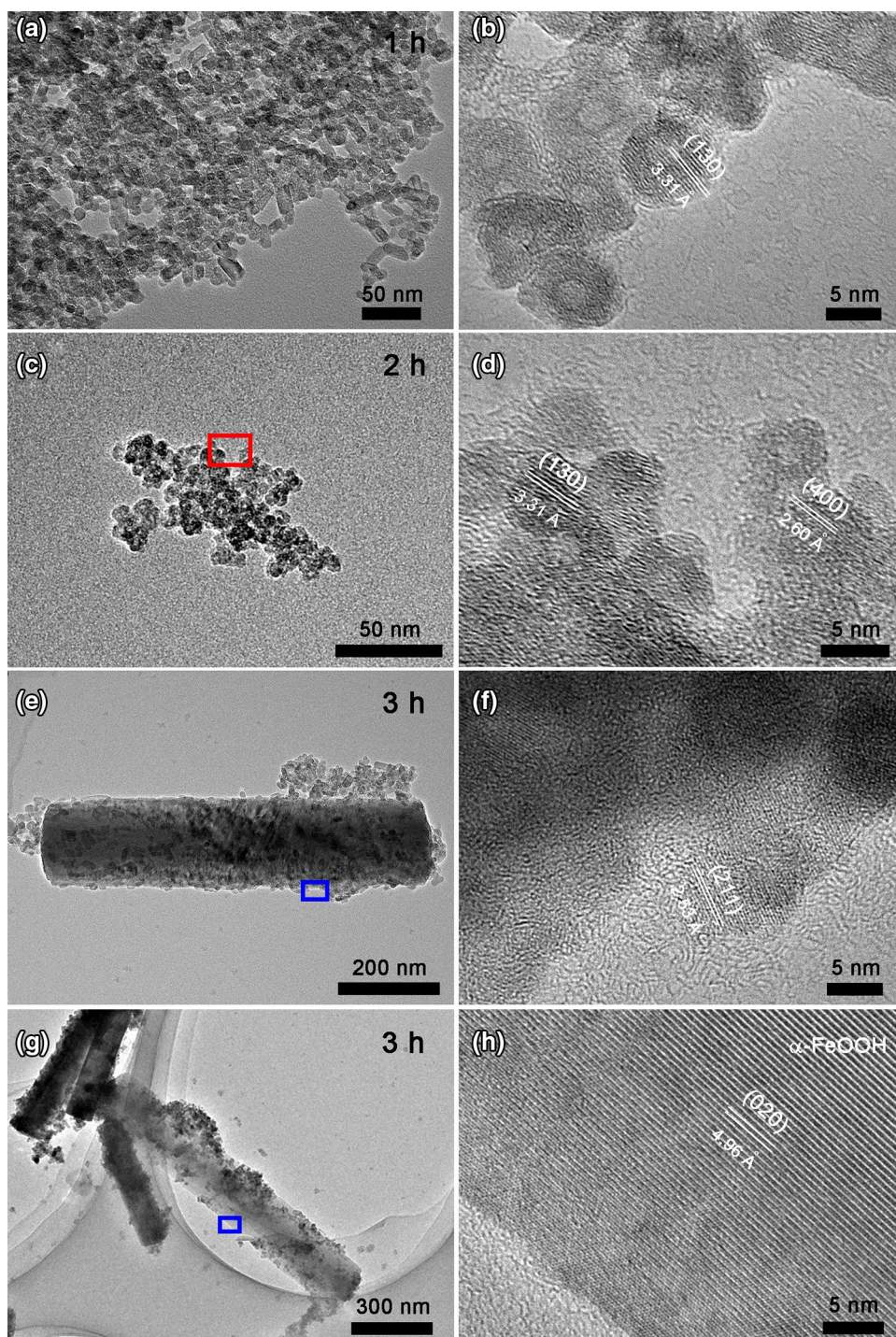
The electrochemical properties of  $\alpha$ -FeOOH CTPs were studied, as shown in Fig. 10. Figure 10a depicts the initial five CV curves of the  $\alpha$ -FeOOH electrode between 0.01 and 3.0 V (vs.  $\text{Li}^+/\text{Li}$ ). In the first cycle, three reduction peaks and three oxidation peaks can be clearly observed. The small peaks at 1.58 and 0.91 V correspond to the lithium intercalation before the reduction reaction. The apparent reduction peak (0.48 V) corresponds to the process of  $\text{Fe}^0$  embedded in  $\text{Li}_2\text{O}$  and  $\text{LiOH}$  matrix, and the formation of a solid electrolyte interface (SEI) layer [4, 10]. The three oxidation peaks (1.15, 1.73 and 1.88 V) are presumably ascribed to the oxidation of  $\text{Fe}^0$  to  $\text{Fe}_2\text{O}_3$  [41].

Figure 10b displays the discharge–charge profiles for the 1st, 2nd and 3rd cycle at  $100 \text{ mA g}^{-1}$ . The discharge profiles show that voltage plateau during the discharge–charge process is clear, which is in a good agreement with the CV results. The rate capabilities of  $\alpha$ -FeOOH electrodes were examined by charging/discharging at various current densities (Fig. 10c). Obviously, the specific capacities of  $\alpha$ -FeOOH electrodes at current densities of 200, 400, 800, 1000, and 2000  $\text{mA g}^{-1}$  are 955, 860, 743, 668, and 531  $\text{mAh g}^{-1}$ , respectively. The  $\alpha$ -FeOOH CTPs electrode could quickly restore a high reversible capacity of  $920 \text{ mAh g}^{-1}$ , when the current density was reduced back to  $100 \text{ mA g}^{-1}$ . It is worth noting that the electrode still delivers a high discharge capacity of  $\sim 531 \text{ mAh g}^{-1}$  at  $2 \text{ A g}^{-1}$ , which is higher than the theoretical capacity of graphite-based materials ( $372 \text{ mAh g}^{-1}$ ). The cycle performances and coulombic efficiency (CE) of  $\alpha$ -FeOOH CTPs were also evaluated (Fig. 10d). It shows that the  $\alpha$ -FeOOH electrodes could deliver a discharge capacity of  $870 \text{ mAh g}^{-1}$  after 100 cycles. When the electrode was further tested at a higher current density ( $0.5 \text{ A g}^{-1}$ ), it can still deliver a reversible capacity of  $760 \text{ mAh g}^{-1}$ , suggesting good cycling performance of the  $\alpha$ -FeOOH CTPs electrode.

To further study the capacitive behavior of the  $\alpha$ -FeOOH electrodes, their kinetics were analyzed by CV measurements, which were collected after 30 cycles of the charge/discharge process. As clearly shown in Fig. 11a, the CV curves at different sweep rates from 0.1 to  $1.0 \text{ mV s}^{-1}$  display the similar shapes. Normally, the scan rate ( $v$ ) and the measured current ( $i$ ) obey the following relationship [42]:

$$i = av^b$$

**Fig. 7** Time-resolved TEM images from the FeOOH aged at 180 °C with a reaction time of 1 h (a), 2 h (c), and 3 h (e), (g). **b** HRTEM image of the sample taken from (a). **d** HRTEM image of the region enclosed by a red rectangle in (c). **f**, **h** HRTEM images of the region enclosed by a blue rectangle in (e) and (g), respectively. (Color figure online)



where  $a$  and  $b$  are adjustable parameters. The value of  $b$  is determined by the slope of the  $\ln i$  versus  $\ln v$ . When the  $b$  value approaches to 1, the system is mainly controlled by the capacitance process. When the  $b$  value is close to 0.5, the diffusion-controlled process dominates the charge transfer. Figure 11b, c show the  $b$ -values at reduction (0.63–0.8 V) and oxidation (1.62–1.8 V) processes. The lowest  $b$  value is 0.60 for the reduction process and 0.83 for the oxidation

process, which reveals that charge storage partially arises from surface capacitive effect.

To clearly illustrate the capacitance contribution, the total storage of Li ions can be distinguished into two parts. The capacitive contribution is calculated according to the following equation [43]:

$$i = k_1 v + k_2 v^{1/2}$$

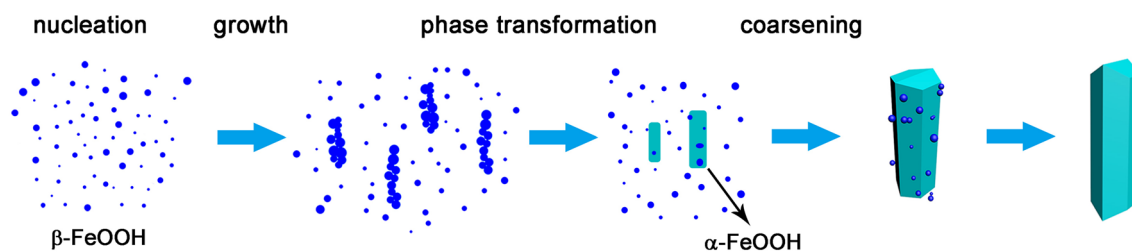


Fig. 8 Schematic illustration of the fabrication process of  $\alpha$ -FeOOH CTPs

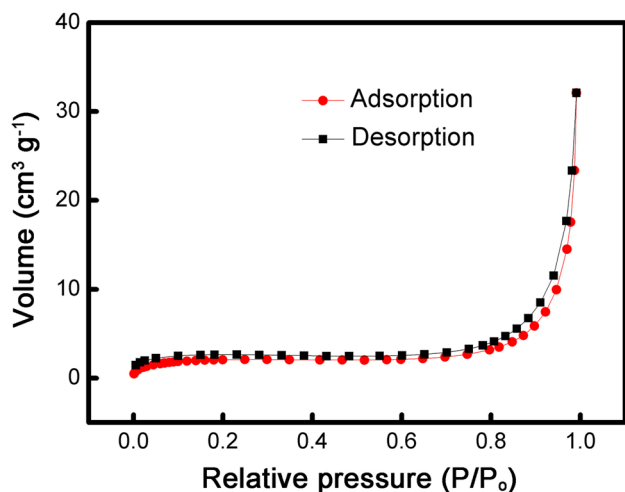


Fig. 9 Nitrogen adsorption/desorption isotherm curves of  $\alpha$ -FeOOH

$k_1v$  and  $k_2v^{1/2}$  represent the surface-capacitive effects and diffusion-controlled redox process, respectively. Therefore, by determining  $k_1$  and  $k_2$ , we can identify the fraction of the current at each specific potential. The values of  $k_1$  and  $k_2$  can be obtained by plotting  $i(V)/v^{1/2}$  versus  $v^{1/2}$ , and thus the capacitive current  $i_c(V) = k_2v$  could be extracted from the total one. Figure 11d shows a typical CV profile for the capacitive current (blue region) compared to the total current. It can be seen that 78% of the total Li-ion storage in the electrode is quantified as capacitive at the sweep rate of  $0.5 \text{ mV s}^{-1}$ , indicating that most of the capacity results from the interface of the electrode. The results reveal that the good Li-ion storage performance of  $\alpha$ -FeOOH electrodes can be attributed to the surface-controlled capacitive behavior.

EIS measurement was conducted to further understand the electrochemical performance. From Fig. 12a, it can be seen that the phase angle at the low frequency is nearly  $73^\circ$ , which confirms the pseudocapacitive feature of the  $\alpha$ -FeOOH electrode. As shown in Fig. 12c, the Nyquist plots are composed of a semicircle at high frequency and a straight line at low frequency [40, 41].  $R_s$  and  $R_{ct}$  represent solution resistance and

charge transfer resistance, CPE is double-layer capacitance,  $C$  is a Faradaic capacitance and  $Z_w$  is the Warburg impedance associated with lithium diffusion. The  $R_{ct}$  of  $\alpha$ -FeOOH electrode is  $117 \Omega$ . Furthermore, the inclined line at low frequency indicates the capacitive-like behavior in the  $\alpha$ -FeOOH electrode. The diffusion coefficient ( $D_{Li}$ ) was calculated using the following equations [44]:

$$D_{Li} = \frac{R^2 T^2}{2A^2 n^4 F^2 C^2 \sigma^2}$$

$$Z_{re} = R_s + R_{ct} + \sigma \omega^{-0.5}$$

where  $R$  is the gas constant,  $T$  is the absolute temperature,  $F$  is the Faraday constant,  $C$  is the concentration of lithium ions,  $A$  is the surface area of the electrode,  $n$  is the number of electrons transferred in the half-reaction, and  $\sigma$  is the Warburg factor which is related to  $Z_{re}$ . Figure 12d shows the graph of  $Z_{re}$  plotted against  $\omega^{-0.5}$ . The  $\sigma$  value of  $\alpha$ -FeOOH electrode is determined to be 58.8. The corresponding lithium-ion diffusion coefficient of  $\alpha$ -FeOOH electrode is calculated to be  $1.09 \times 10^{-14} \text{ cm}^2 \text{ s}^{-1}$ .

To further clarify the electrochemical stability of the  $\alpha$ -FeOOH prism, the microstructural evolution after 100 cycles was investigated using TEM, as shown in Fig. 13. From Fig. 13a, b, the initial morphology of  $\alpha$ -FeOOH is well maintained, indicating excellent structural stability during the cycle. The top-ending of the prisms with canted facets is also maintained. As shown in Fig. 13c, d, a porous pulverized morphology is observed, which is assembled from a plurality of nanocrystals with a size of  $\sim 5 \text{ nm}$ . After several cycles, the  $\alpha$ -FeOOH electrode undergoes a transition from single crystalline to polycrystalline. These resulting crystallites can provide more diffusion channels and reaction sites for lithium ions than previous single crystal states [8, 10, 12]. Therefore, the  $\alpha$ -FeOOH electrode could exhibit higher surface capacitive capacity for lithium storage during the charge/discharge process. This advantage can provide strong support for improving the lithium storage performance of the  $\alpha$ -FeOOH.

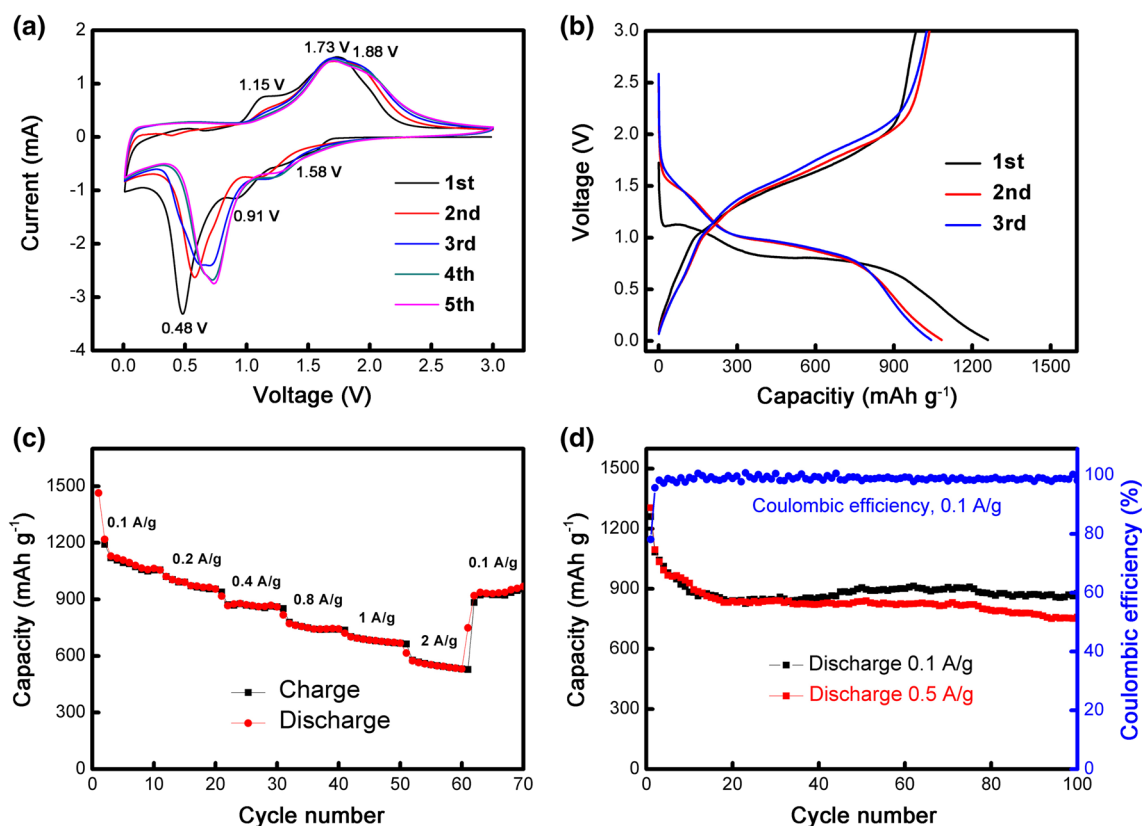


**Fig. 10** Electrochemical performances of  $\alpha$ -FeOOH CTPs. **a** CV curves at a scanning rate of  $0.5 \text{ mV s}^{-1}$  with a voltage window of 0.01–3.0 V. **b** galvanostatic charge/discharge profiles. **c** rate performance. **d** cycling performance at 0.1 and 0.5  $\text{A g}^{-1}$  and the coulombic efficiency

**Fig. 11** **a** CV curves of the cell after 30 cycles at different sweep rates. **b** The  $b$  values of the electrode over various cathodic peaks. **c** The  $b$  values of the electrode over various anodic peaks. **d** Separation of the capacitive and diffusion currents at a scan rate of  $0.5 \text{ mV s}^{-1}$ , and the capacitive contribution to the total current is shown by the blue region. (Color figure online)

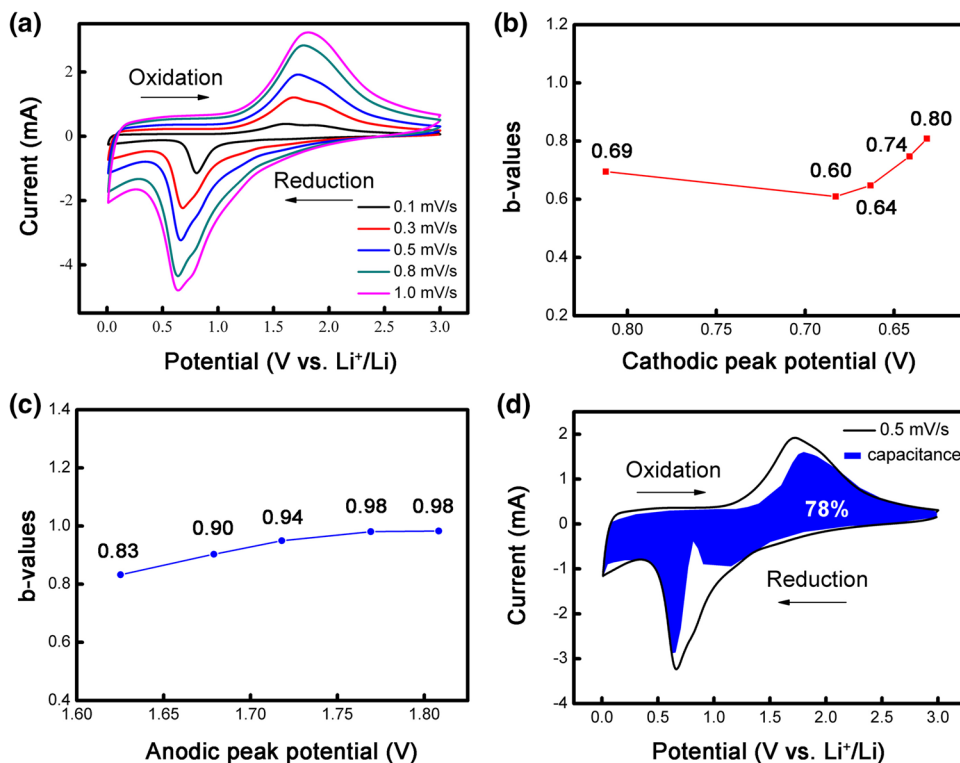


**Fig. 12** **a, b** Bode phase angle and bode magnitude diagrams for  $\alpha$ -FeOOH electrode. **c** EIS of  $\alpha$ -FeOOH electrode. The inset is the equivalent circuit model. **d** Graph of  $Z_{re}$  plotted against  $\omega^{-0.5}$

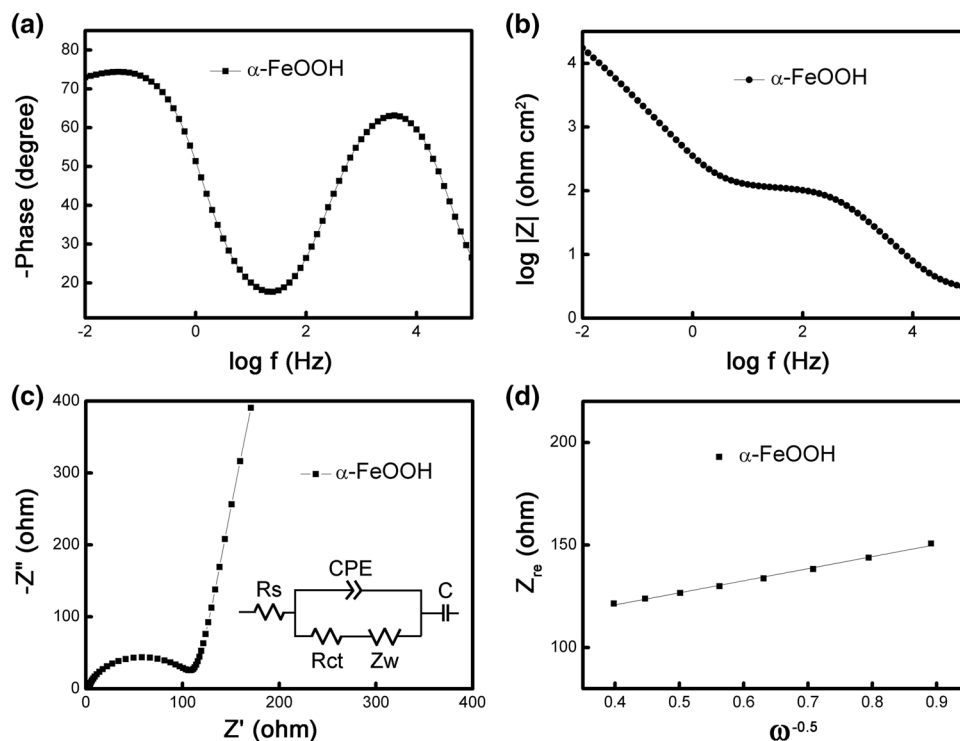
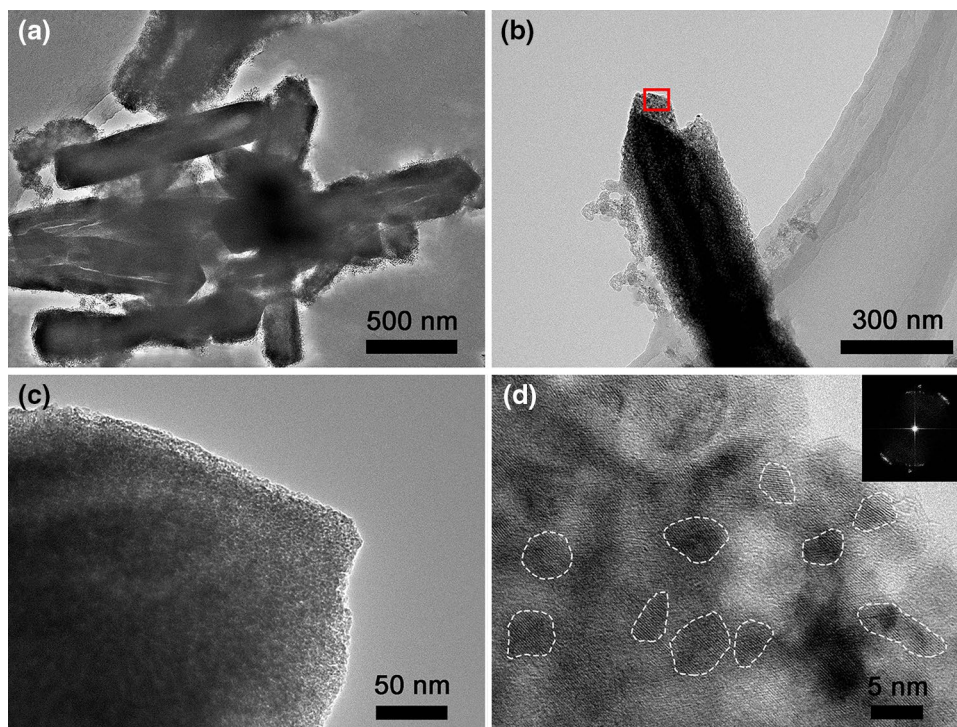


**Fig. 13** **a, b** and **c** Ex-situ TEM images of  $\alpha$ -FeOOH electrodes after the 100th cycle at  $100 \text{ mA g}^{-1}$ . **d** HRTEM image of the  $\alpha$ -FeOOH electrodes taken from **(b)**. Inset is corresponding FFT



## 4 Conclusions

In summary,  $\alpha$ -FeOOH CTPs with a length of about  $1 \mu\text{m}$  and a width of about  $200 \text{ nm}$  are obtained by hydrothermal treatment. The single-crystalline  $\alpha$ -FeOOH CTP is

enclosed by six symmetrical side facets, two  $\{020\}$  and four  $\{110\}$ . Depending on the reaction time, two different top-endings (one flat or two canted facets) are obtained. Phase transformation from tetragonal  $\beta$ -FeOOH to orthorhombic  $\alpha$ -FeOOH is observed during the growth process. When

evaluated as anode materials of LIBs, the  $\alpha$ -FeOOH electrode delivers a stable capacity of 870, 760 mAh g<sup>-1</sup> at 100, 500 mA g<sup>-1</sup>, respectively. The synthesized CTP contributes to structural stability during Li<sup>+</sup> insertion/extraction process. Moreover, porous pulverized morphology is found during the charge/discharge process, which exhibits surface-controlled capacitive behavior in the electrode system. These advantages contribute to the improvement of the electrochemical properties of  $\alpha$ -FeOOH.

**Acknowledgements** The authors would like to thank the financial support from the National Natural Science Foundation of China (Grant Nos. 10974105, 21701095), Natural Science Foundation of Shandong Province, China (Grant No. ZR2017BEM007), Program of Science and Technology for Higher Education in Shandong Province, China (Grant No.:J17KA010), China Postdoctoral Science Foundation (Grant No. 2017M622131), and High-end Foreign Experts Recruitment Programs (Grant Nos. GDW20163500110 and GDW20173500154). Y. Q. Wang would also like to thank the financial support from the Top-notch Innovative Talent Program of Qingdao City (Grant No. 13-CX-08), the Taishan Scholar Program of Shandong Province, and Qingdao International Center for Semiconductor Photoelectric Nanomaterials and Shandong Provincial University Key Laboratory of Optoelectrical Material Physics and Devices.

## References

- Armand M, Tarascon JM (2008) Building better batteries. *Nature* 451:652–657
- Wang ZY, Zhou L, Low XW (2012) Metal oxide hollow nanostructures for lithium-ion batteries. *Adv Mater* 24:1903–1911
- Yu S, Lee SH, Lee DJ, Sung Y, Hyeon T (2016) Conversion reaction-based oxide nanomaterials for lithium ion battery anodes. *Small* 12:2146–2172
- Navrotsky A, Mazeina L, Majzlan J (2008) Size-driven structural and thermodynamic complexity in iron oxides. *Science* 319:1635–1638
- Zhang L, Wu HB, Lou XW (2014) Iron-oxide-based advanced anode materials for lithium-ion batteries. *Adv Energy Mater* 4:1300958
- Zheng F, He M, Yang Y, Chen Q (2015) Nano electrochemical reactors of Fe<sub>2</sub>O<sub>3</sub> nanoparticles embedded in shells of nitrogen-doped hollow carbon spheres as high-performance anodes for Lithium-ion batteries. *Nanoscale* 7:3410–3417
- Imtiaz M, Chen Z, Zhu CL, Pan H, Zada I, Li Y, Bokhari SW, Luan RY, Nigar S, Zhu SM (2018) In situ growth of  $\beta$ -FeOOH on hierarchically porous carbon as anodes for high-performance lithium-ion batteries. *Electrochim Acta* 283:401–409
- Bhuvaneshwari S, Pratheeksha PM, Anandan S, Rangappa D, Gopalan R, Rao TN (2014) Efficient reduced graphene oxide grafted porous Fe<sub>3</sub>O<sub>4</sub> composite as a high performance anode material for Li-ion batteries. *Phys Chem Chem Phys* 16:5284–5294
- Qi H, Cao L, Li J, Huang J, Xu Z, Cheng Y, Kong X, Yanagisawa K (2016) High pseudocapacitance in FeOOH/rGO composites with superior performance for high rate anode in Li-ion battery. *ACS Appl Mater Interfaces* 8:35253–35263
- Zhai Y, Xu L, Qian Y (2016) Ce-doped  $\alpha$ -FeOOH nanorods as high-performance anode material for energy storage. *J Power Sources* 327:423–431
- Yu LH, Xi SB, Wei C, Zhang WY, Du YH, Yan QY, Xu ZC (2015) Superior lithium storage properties of  $\beta$ -FeOOH. *Adv Energy Mater* 5:1401517
- Yu LH, Wei C, Yan QY, Xu ZJ (2015) Controlled synthesis of high-performance  $\beta$ -FeOOH anodes for lithium-ion batteries and their size effects. *Nano Energy* 13:397–404
- Wu R, Wang DP, Rui XH, Liu B, Zhou K, Law AWK, Yan QY, Wei J, Chen Z (2015) In-situ formation of hollow hybrids composed of cobalt sulfides embedded within porous carbon polyhedra/carbon nanotubes for high-performance lithium-ion batteries. *Adv Mater* 27:3038–3044
- Wu R, Qian X, Zhou K, Wei J, Lou J, Ajayan PM (2014) Porous spinel Zn<sub>x</sub>Co<sub>3-x</sub>O<sub>4</sub> hollow polyhedra templated for high-rate lithium-ion batteries. *ACS Nano* 8:6297–6303
- Liu DQ, Wang X, Wang XB, Tian W, Bando Y, Golberg D (2013) Co<sub>3</sub>O<sub>4</sub> nanocages with highly exposed {110} facets for high-performance lithium storage. *Sci Rep* 3:2543
- Kakuta S, Numata T, Okayama T (2014) Shape effects of goethite particles on their photocatalytic activity in the decomposition of acetaldehyde. *Catal Sci Technol* 4:164–169
- Frost R, Zhu H, Wu P, Bostrom T (2005) Synthesis of acicular goethite with surfactants. *Mater Lett* 59:2238–2241
- Meng F, Morin S, Jin S (2011) Rational solution growth of  $\alpha$ -FeOOH nanowires driven by screw dislocations and their conversion to  $\alpha$ -Fe<sub>2</sub>O<sub>3</sub> nanowires. *J Am Chem Soc* 133:8408–8411
- Geng FX, Zhao ZG, Cong HT, Geng JX, Cheng HM (2006) An environment-friendly microemulsion approach to  $\alpha$ -FeOOH nanorods at room temperature. *Mater Res Bull* 41:2238–2243
- Zhu T, Chen JS, Lou XW (2011) Glucose-assisted one-pot synthesis of FeOOH nanorods and their transformation to Fe<sub>3</sub>O<sub>4</sub>@carbon nanorods for application in lithium ion batteries. *J Phys Chem C* 115:9814–9820
- Varanda LC, Morales MP, Jafelicci JM, Serna CJ (2002) Monodispersed spindle-type goethite nanoparticles from Fe<sup>III</sup> solutions. *J Mater Chem* 12:3649–3653
- Liang H, Chen W, Wang R, Qi Z, Mi J, Wang Z (2015) X-shaped hollow  $\alpha$ -FeOOH penetration twins and their conversion to  $\alpha$ -Fe<sub>2</sub>O<sub>3</sub> nanocrystals bound by high-index facets with enhanced photocatalytic activity. *Chem Eng J* 274:224–230
- Zhang CM, Zhu JX, Rui XH, Chen J, Sim DH, Shi WH, Hng HH, Lim TM, Yan QY (2012) Synthesis of hexagonal-symmetry  $\alpha$ -iron oxyhydroxide crystals using reduced graphene oxide as a surfactant and their Li storage properties. *CrystEngComm* 14:147–153
- Granados-Correa F, Corral-Capulin NG, Olguín MT, Acosta-León CE (2011) Comparison of the Cd(II) adsorption processes between boehmite ( $\gamma$ -AlOOH) and goethite ( $\alpha$ -FeOOH). *Chem Eng J* 171:1027–1034
- Mao XB, Yang HC, Zhou XM, Wang CX, Wnag YS, Yang YL, Wnag C, Liu G (2010) Straight and branched goethite topology by oriented attachment at high pH. *Cryst Growth Des* 10:504–509
- Lin M, Tng L, Lim T, Choo M, Zhang J, Tan HR, Bai S (2014) Hydrothermal synthesis of octadecahedral hematite ( $\alpha$ -Fe<sub>2</sub>O<sub>3</sub>) nanoparticles: an epitaxial growth from goethite ( $\alpha$ -FeOOH). *J Phys Chem C* 118:10903–10910
- Chun C, Penn RL, Arnold WA (2006) Kinetic and microscopic studies of reductive transformations of organic contaminants on goethite. *Environ Sci Technol* 40:3299–3304
- Jolivet JP, Chanéac C, Tronc E (2004) Iron oxide chemistry: from molecular clusters to extended solid networks. *Chem Commun* 35:477–483
- Almeida TP, Fay MW, Zhu Y, Brown PD (2010) A valve-assisted snapshot approach to understand the hydrothermal synthesis of  $\alpha$ -Fe<sub>2</sub>O<sub>3</sub> nanorods. *CrystEngComm* 12:1700–1704

30. Wei C, Nan Z (2011) Effects of experimental conditions on one-dimensional single-crystal nanostructure of  $\beta$ -FeOOH. *Mater Chem Phys* 127:220–226
31. Morterra C, Chiorlino A, Borello E (1984) An IR spectroscopic characterization of  $\alpha$ -FeOOH (goethite). *Mater Chem Phys* 10:119–138
32. Liang J, Luo M, Yang C, Fang J, Li L (2011) Synthesis of spindle-shaped  $\alpha$ -FeOOH and  $\alpha$ -Fe<sub>2</sub>O<sub>3</sub> nanocrystals. *Cryst Res Technol* 46:493–496
33. Frandsen C, Legg BA, Comolli LR, Zhang HZ, Gilbert B, Johnson E, Banfield JF (2014) Aggregation-induced growth and transformation of  $\beta$ -FeOOH nanorods to micron-sized  $\alpha$ -Fe<sub>2</sub>O<sub>3</sub> spindles. *CrystEngComm* 16:1451–1458
34. Burleson DJ, Penn RL (2006) Two-step growth of goethite from ferrihydrite. *Langmuir* 22:402–409
35. Guyodo Y, Mostrom A, Penn RL, Banerjee SK (2003) From nanodots to nanorods: oriented aggregation and magnetic evolution of nanocrystalline goethite. *Geophys Res Lett* 30:405–414
36. Banfield JF, Welch SA, Zhang HZ, Ebert TT, Penn RL (2000) Aggregation-based crystal growth and microstructure development in natural iron oxyhydroxide biomineralization products. *Science* 289:751–754
37. Burrows ND, Kesselman E, Sabyrov K, Stemig A, Talmon Y, Penn RL (2014) Crystalline nanoparticle aggregation in non-aqueous solvents. *CrystEngComm* 16:1472–1481
38. Raming TP, Winnubst AJA, van Kats CM, Philipse AP (2002) The synthesis and magnetic properties of nanosized hematite ( $\alpha$ -Fe<sub>2</sub>O<sub>3</sub>) particles. *J Colloid Interface Sci* 249:346–350
39. Wiogo H, Lim M, Munroe P, Amal R (2011) Understanding the formation of iron oxide nanoparticles with acicular structure from iron(III) chloride and hydrazine monohydrate. *Cryst Growth Des* 11:1689–1696
40. Lou X, Wu X, Zhang Y (2009) Goethite nanorods as anode electrode materials for rechargeable Li-ion batteries. *Electrochem Commun* 11:1696–1699
41. Wang J, Polleux J, Lim J, Dunn B (2007) Pseudocapacitive contributions to electrochemical energy storage in TiO<sub>2</sub> anatase nanoparticles. *J Phys Chem C* 111:14925–14931
42. Chao D, Zhu C, Yang PH, Xia XH, Liu JL, Wang J, Fan XF, Savilov SV, Lin J, Fan HJ, Shen ZX (2016) Array of nanosheets render ultrafast and high-capacity Na-ion storage by tunable pseudocapacitance. *Nature Commun* 7:12122
43. Shenouda AY, Liu HK (2008) Electrochemical behavior of tin borophosphate negative electrodes for energy storage systems. *J Power Sources* 185:1386–1391

**Publisher's Note** Springer Nature remains neutral with regard to jurisdictional claims in published maps and institutional affiliations.

## Affiliations

Huanqing Liu<sup>1</sup> · Jiajia Zou<sup>1</sup> · Yanhua Ding<sup>1</sup> · Bing Liu<sup>1</sup> · Yiqian Wang<sup>1</sup> 

<sup>1</sup> College of Physics, Qingdao University, No. 308 Ningxia Road, Qingdao 266071, People's Republic of China